

7 Submillimeter Telescopes

Thomas G. Phillips¹ · Stephen Padin² · Jonas Zmuidzinas³

¹Physics, Mathematics & Astronomy, California Institute of Technology, Pasadena, CA, USA

²California Institute of Technology, Pasadena, CA, USA


³George W. Downs Laboratory of Physics, California Institute of Technology, Pasadena, CA, USA


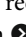
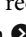
1	Introduction	284
2	Submillimeter Detection	289
2.1	Heterodyne Detectors	290
2.1.1	Hot Electron Bolometers	290
2.1.2	SIS Detectors	292
3	Telescopes	296
3.1	Optics	296
3.1.1	Cassegrain and Gregory Telescopes	296
3.1.2	Plate Scale	300
3.1.3	Other Telescope Designs	301
3.1.4	Chopping and Scanning	301
3.1.5	Scattering and Loss	302
3.1.6	Optical Components	302
3.2	Structure and Mechanics	302
3.2.1	Pointing and Wavefront Errors	303
3.2.2	Primary Mirror Support	304
3.2.3	Mirror Control	306
3.2.4	Telescope Mount	307
3.3	Alignment	309
	References	311

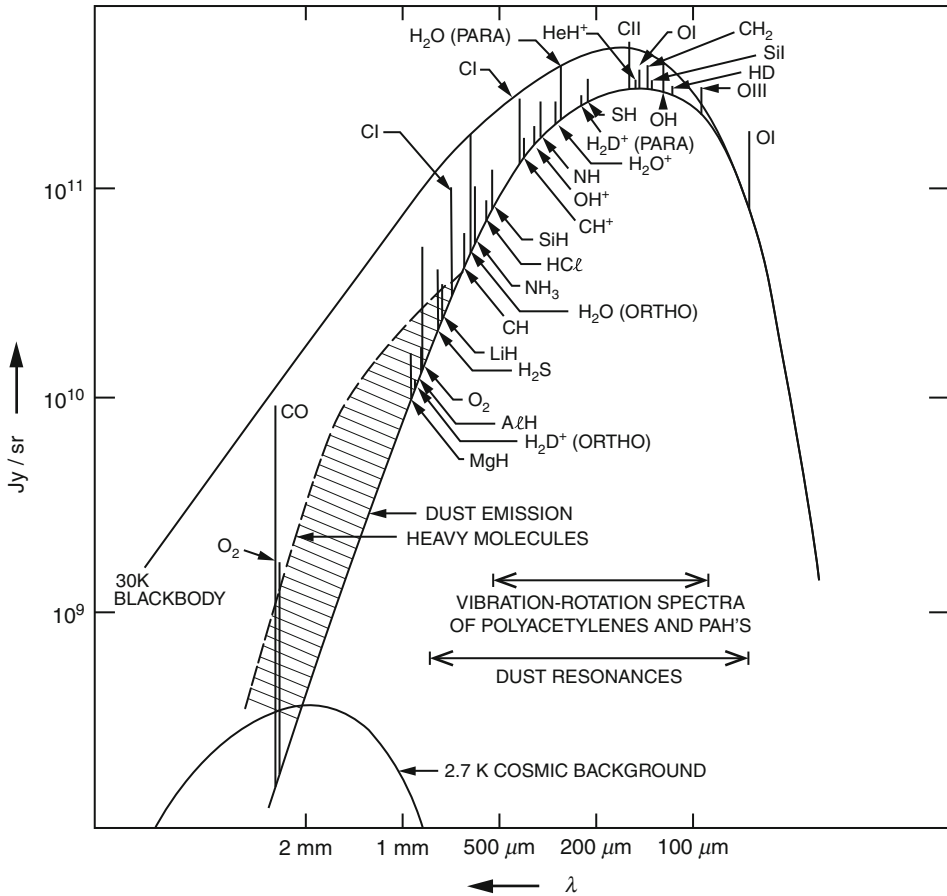
List of Abbreviations: *CFRP*, Carbon fiber reinforced plastic; *CMB*, Cosmic microwave background; *FOV*, Field of view; *PSF*, Point spread function; *RC*, Ritchey-Chrétien

1 Introduction

The submillimeter band is a critical one for astronomy. It contains spectral and spatial information on very distant newly formed galaxies and on the early stages of star formation within gas clouds. Yet it is one of the few regions of the electromagnetic spectrum still to be made fully available to astronomy. This is in part due to the general difficulties of construction of detectors, receivers, and telescopes for these wavelengths and in part to the attenuating nature of the Earth's atmosphere. In recent years, optical style telescopes have become available, either on high mountain sites, or in the case of the NASA Kuiper Airborne Observatory (KAO) or Stratospheric Observatory for Infrared Astronomy (SOFIA) on board a high-altitude airplane. The James Clerk Maxwell telescope at 15 m and the Caltech Submillimeter Observatory (CSO) telescope at 10.4 m are both large enough to have developed the field. However, the ESA satellite Herschel has now provided the required space platform for complete spectral coverage and the Atacama Large Millimeter/Submillimeter Array (ALMA) the high spatial resolution, aperture synthesis, high-sensitivity platform.

On the whole, the emission strength is low in the submillimeter for astronomical objects. The electronic processes which provide strong emission in the radio fade away at high frequencies, and the thermal emission from cold objects is relatively weak, particularly when highly redshifted. An overall view of the spectrum of a dense interstellar cloud in our own galaxy provides a sense of the spectroscopic requirements.  *Figure 7-1* shows a schematic representation of the likely emission from a typical star-forming cloud in the galaxy. The cloud dust and gas temperatures are assumed to be 30 K. A black body curve provides an upper bound to the emission strength, apart from possible maser action which is ignored here. Dust is optically thick at short wavelengths, and the continuum emission from it lies on the black body curve, but drops well below at long wavelengths where the dust is optically thin. At millimeter wavelengths the gas spectrum is dominated by emission due to the rotation spectrum of heavy molecules. The strongest of these by far is that of the carbon monoxide (CO) molecule which is so abundant that it can have optical depths of ~ 100 , even though it has a dipole moment of only ~ 0.12 debye. Low-lying transitions of CO usually reflect the gas temperature and are represented in the figure as reaching the black body curve, at least for the line centers. However, for high values of the rotational quantum number (J), the molecules tend to be deexcited and emit less strongly, so the line intensities drop below the black body curve.

An actual example of part of the millimeter band spectrum of the Orion Cloud (OMC-1) with the continuum removed is shown in  *Fig. 7-2*. This was taken with one of the Leighton Caltech telescopes using an SIS (see  *Sect. 2*) receiver (Blake et al. 1987). The result was the detection of about 1,000 lines which were identified as various transitions of about 30 molecules, varying in complexity from CO to dimethyl ether (CH_3OCH_3). The spectrum observed was about 60 GHz in width which permitted multiline observations of the molecules so necessary for secure identification. It is clear that providing a large instantaneous bandwidth is a primary requisite of a millimeter or submillimeter receiver system. Much higher spectral resolution is available. An expanded region is shown in  *Fig. 7-3*. It turns out that several different spatial

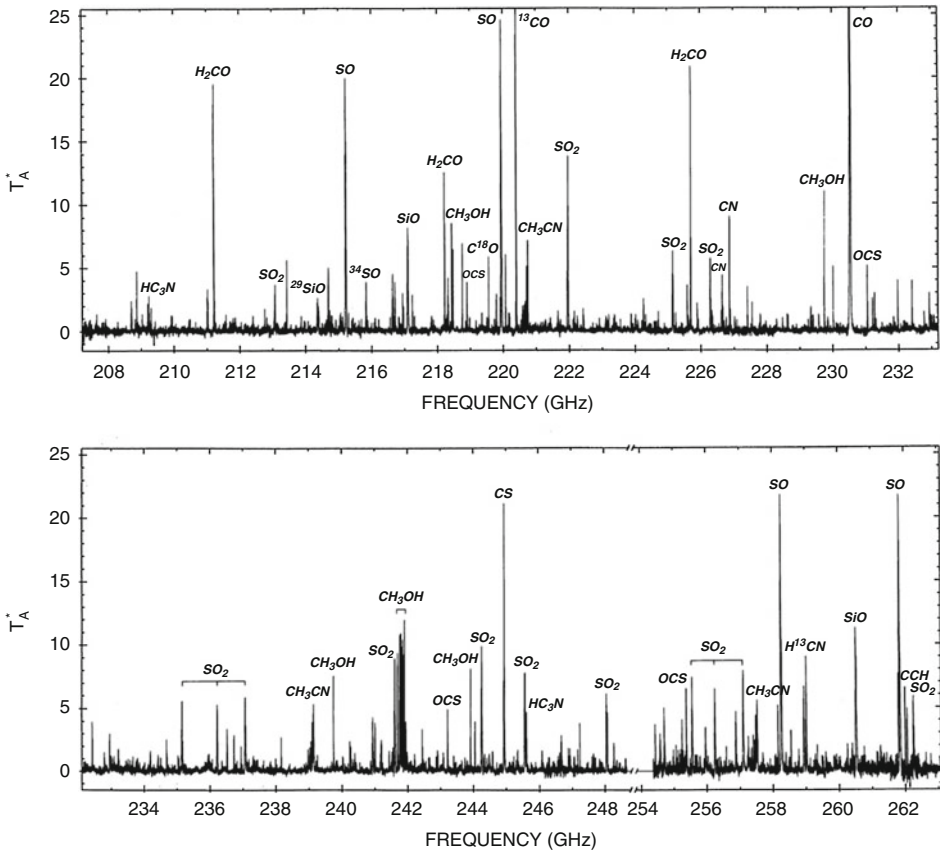


■ Fig. 7-1

The anticipated spectrum of a 30 K cloud, showing the dust emission, the heavy molecule line forest, and, at high frequencies, the fast rotating light hydrides (Phillips and Keene 1992)

objects, within the one telescope beam, can be discriminated by their distinctive line shapes. This emphasizes a second requirement for interstellar spectroscopy, namely, very good spectral resolution.

Returning to [Fig. 7-1](#), as we move from the millimeter band, containing many lines of heavy molecules, to the submillimeter, we find that the spectrum is dominated by light molecules containing hydrogen. These light molecules have small moments of inertia and therefore rotate fast, so their fundamental rotation lines appear in the submillimeter. Heavy molecule lines become less important due to the de-excitation suffered by a molecule in a high J energy level, well above the ground state. The postulation of [Fig. 7-1](#) has been verified by the space project, HIFI, on the Herschel telescope orbiting at the L2 point. Many transition lines were recently discovered by the HIFI instrument, under the water lines which prevent observations from even high mountain sites. An example is HF ([Fig. 7-4](#)) and water itself was seen, initially for weak lines for which the atmosphere is not opaque, mostly from the KAO. More recently,



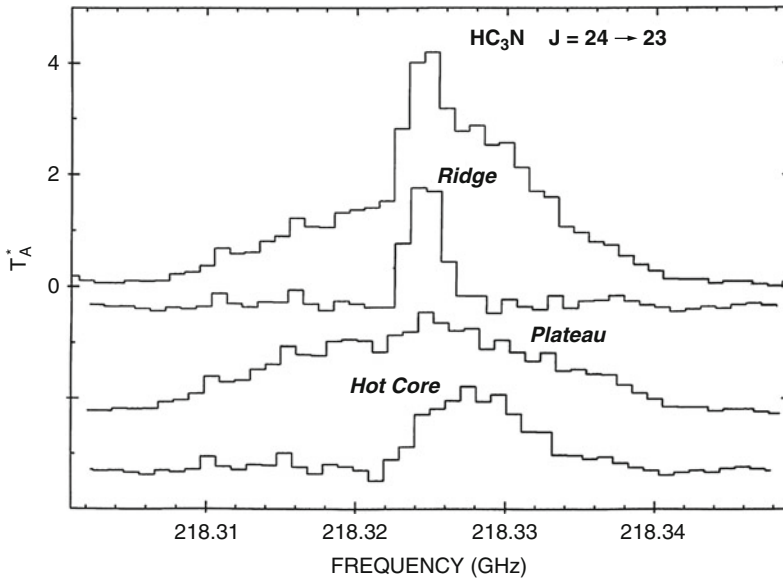
■ Fig. 7-2

Part of the heavy molecule spectrum as seen from the first Leighton telescope in Blake's thesis

it was seen from space probes such as SWAS and finally, definitively, with HIFI. Although it is clear from [Fig. 7-1](#) that there is a tremendous quantity of astrophysical information contained in the submillimeter band, it has proved hard to obtain, even for our own galaxy, because of the interfering effects of the Earth's atmosphere.

[Figure 7-5](#) shows the transmission for good weather (about 1 mm of precipitable water) at the 4,200-m level on Mauna Kea for the submillimeter band. There are three useful regions: the radio/millimeter region from 0 to 300 GHz which is almost completely transparent, apart from a few O_2 and H_2O lines, and the two wide submillimeter windows at roughly 650 GHz ($\sim 450 \mu\text{m}$) and 850 GHz ($\sim 350 \mu\text{m}$). The rest of the spectrum is blacked out by water lines, apart from some narrow windows near 400 GHz. The atmosphere is completely black at shorter wavelengths until the mid-infrared windows at $\sim 30 \mu\text{m}$ are reached.

At airborne altitudes, say 12,000 m for SOFIA, the transmission is much better, but also not perfect. Several of the lines of [Fig. 7-1](#) were initially detected with early versions of submillimeter detectors from the KAO, such as the fundamental rotation lines of NH_3 (Keene et al. 1983) and HCl (Blake et al. 1985). Many of the high-frequency lines of CO (Phillips et al. 1980a) were observed and some lines of OH and CH (Stacey et al. 1987; Storey et al. 1981).



■ Fig. 7-3

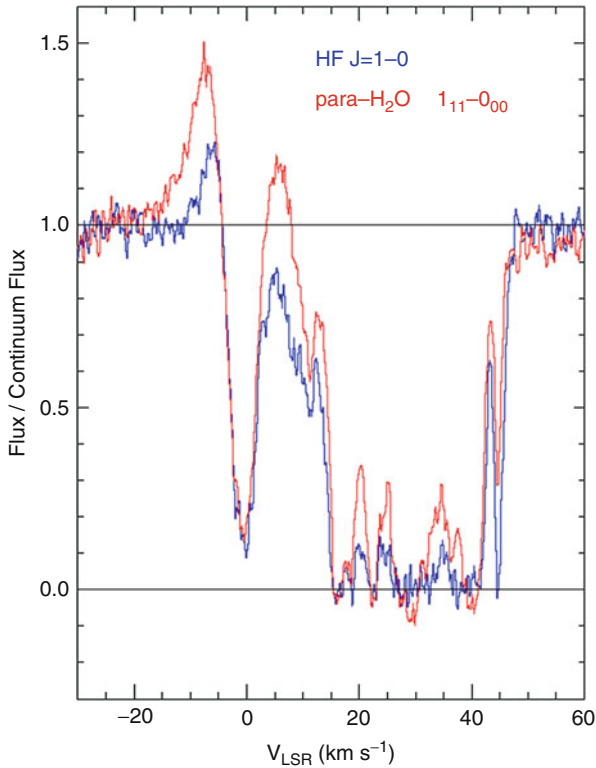
The Orion “hot core,” “Plateau” (outflow), and quiescent “ridge”

Also the atomic fine structure lines of carbon and ionized carbon have been detected by various techniques (Jaffe et al. 1985; Phillips and Huggins 1981; Russell et al. 1980).

With the advent of the mountain-sited submillimeter telescopes and new space-based telescopes, the quality of submillimeter spectroscopy has surpassed that of the millimeter spectrum of Fig. 7-2. An example of the modern line surveys (HIFI) is shown in Fig. 7-6. The data is taken double sideband but deconvolved to single sideband. In actuality, these spectra include common molecules with so many lines that they have to be subtracted in order to see the underlying spectrum. They are designated as “weeds” (an example is CH_3OH).

Being situated between the radio and infrared fields, submillimeter astronomy has naturally borrowed its techniques from these more established areas. The radio is generally considered to be a thermally dominated regime, i.e., $kT > h\nu$; the thermal energy is greater than the photon energy. By contrast, the infrared or optical regimes are in the limit where quantum energies dominate thermal. In the submillimeter, neither thermal effects nor quantum effects can necessarily be assumed negligible and so both must be considered when designing detectors. The two basic methods of detection to be compared are the infrared technique of direct detection, such as bolometric or photodetection, and the radio technique of heterodyne mixing which has been so successful in the millimeter and submillimeter bands. We can make the comparison for a range of required spectral resolutions and astronomical conditions (Phillips 1988). The radio approximation $kT \gg h\nu$ is often used, even though it is not fully valid.

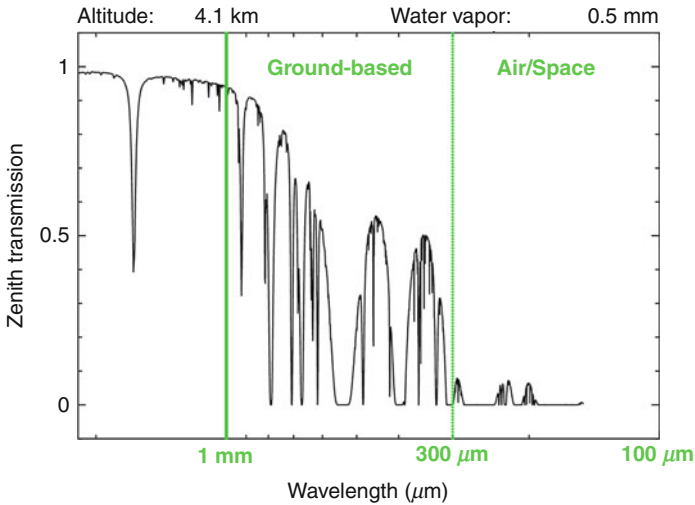
There are clearly two types of science that can be carried out in the submillimeter; continuum observation of dust and high spectral resolution measurements of atomic and molecular line features. The importance of the dust observation became clear when Michael Rowan-Robinson (Rowan-Robinson et al. 1991) found that the IRAS object F10214 was at a large distance ($z = 2.3$). The bolometers in use were the doped Ge type, developed by Frank Low (1961).



■ Fig. 7-4

HF is a strongly bonded, fast-rotating molecule, which is often seen in absorption, and in hot dense regions in emission (Neufeld et al. 2010) and a water absorption spectrum for comparison. The spectra are very similar as seen when the frequencies of observation are shifted to allow this comparison

◆ Figure 7-7 shows a photograph of Phillips and Huggins with the initial InSb hot electron bolometer (see ◆ Sect. 2) receiver mounted at the prime focus of the 200-in. telescope (Phillips et al. 1977). Due to the water and oxygen in the Earth's atmosphere, work from the ground becomes very difficult in the submillimeter, and, as a result, some initial effort was switched to operation on the KAO. Flying at an altitude of 40,000 feet effectively reduced the attenuation by the atmosphere to a reasonable value and allowed observations at much higher frequencies. These included the detection of the CO (4–3) line at 460 GHz (Phillips et al. 1980a); the ground state fine-structure line of atomic carbon (C I) at 492 GHz (Phillips et al. 1980b); the fundamental rotational line of ammonia, NH₃ (1–0) at 572 GHz (Keene et al. 1983); the fundamental rotational line of HCl (1–0) at 626 GHz (Blake et al. 1985); etc. The telescope was small (91.5 cm) but served the purpose of allowing the discovery of many of the molecular and atomic species present in the dense interstellar medium. This work has been now superseded by the SIS receivers (see ◆ Sect. 2) on HIFI/Herschel and SOFIA. SIS receivers also were chosen for ALMA, probably the outstanding astronomy instrument of the decade.



■ Fig. 7-5

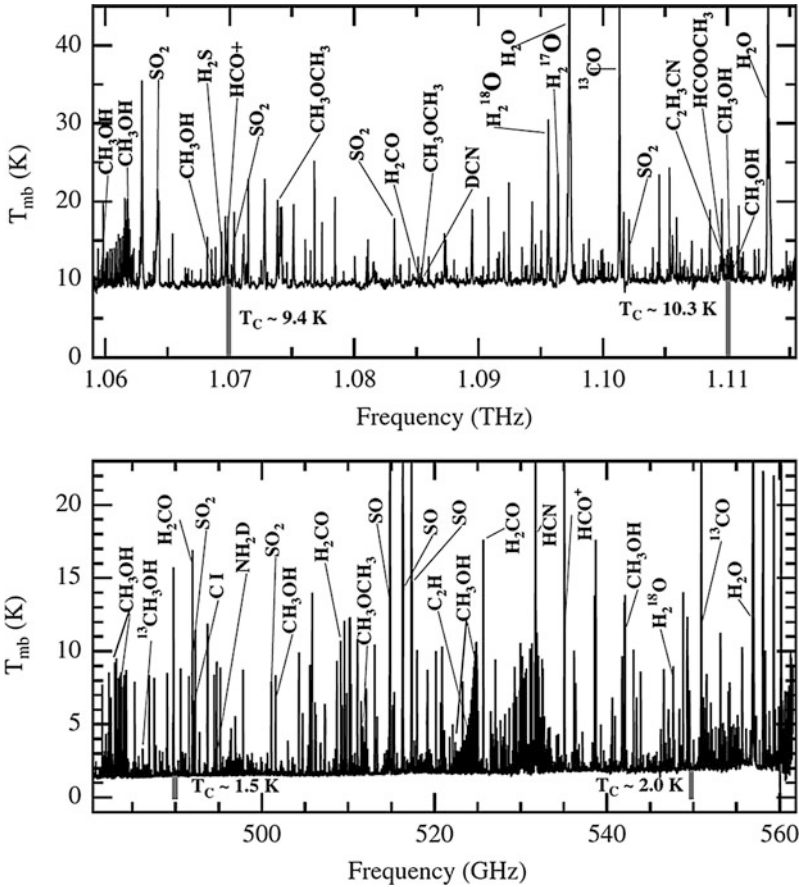
The Earth's atmospheric transmission in the submillimeter band as seen from the CSO. A suitable platform for the various frequency ranges is shown in *green*

2 Submillimeter Detection

There are two basic techniques for millimeter and submillimeter detection. The first is direct detection with a bolometer or photodetector device, and the second is heterodyne detection using a mixer device. Although modern bolometers are more sensitive than mixers, it is still necessary to use mixers where it is required to keep track of phase, e.g., for interferometers, or where very high spectral resolution is needed. Bolometer direct detection requires a detection element such as resistance or reactance which is a function of temperature. If the element has a sufficiently rapid function of temperature that the signal voltage across the device is very much larger than all locally generated noise voltages (e.g., Johnson noise or thermal fluctuation noise), then the signal to noise ratio (S/N) is determined by the background noise. By contrast, the heterodyne process is limited by quantum noise ($\sim h\nu/k$) which is a linear function of frequency. Thus, in general, one can say that direct detection is preferred at infrared wavelengths, and heterodyne techniques are preferred in the radio. In a given case, where noise is determined by the detector element, a comparison will depend on the channel width ($\Delta\nu$), the noise equivalent power (NEP) of the direct detector, and the noise temperature of the heterodyne instrument (T_N) as:

$$\frac{(S/N)_{\text{heterodyne}}}{(S/N)_{\text{direct}}} = \frac{\text{NEP}}{2kT_N\sqrt{\Delta\nu}}$$

In the case where the background is dominant, this ratio depends only on the root of the ratio of channel widths (Phillips 1988).



■ Fig. 7-6

A line survey of Orion using HIFI. The spectrum is amazingly complicated

2.1 Heterodyne Detectors

2.1.1 Hot Electron Bolometers

Any power detector, such as a bolometer, acts to detect the square of the total electric field and can therefore act as a mixer. It comes in two forms, semiconducting and superconducting. First, came the semiconducting device (Phillips and Jefferts 1973). This surprising simple detector was a rod of indium antimonide (InSb) mounted in the E-field of a full-height waveguide with a directly coupled baseband IF amplifier. The device was matched to the waveguide using an E-H tuner in front and a backshort behind. The waveguide device was mounted in a liquid helium cryostat resulting in the first very low temperature mixer receiver for millimeter or submillimeter astronomy. The way in which this hot electron bolometer worked was to absorb the incoming photons via the electron gas and make use of the temperature variation of the electron resistance due to the fact that the resistance was caused by impurity scattering of the



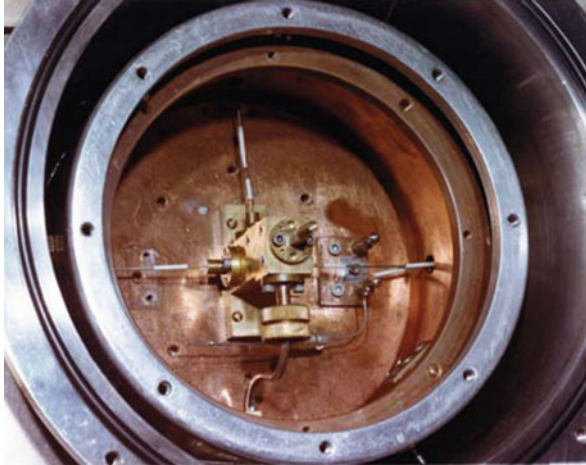
■ Fig. 7-7

Phillips and Huggins at the prime focus of the Palomar 200'' with the InSb hot electron bolometer

Rutherford type. The scattering is less effective as the electrons speed up resulting in a temperature dependence of the resistance. The original mounting scheme showing a scalar feedhorn, a 20-dB coupler for the local oscillator, and various waveguide tuners is displayed in [▶ Fig. 7-8](#).

The simple InSb detector really opened up the millimeter and submillimeter field of interstellar spectroscopy in spite of the very small IF bandpass (~ 1 MHz). This bandpass is set by the relaxation rate of the hot electrons excited by the DC bias. If the astronomical spectrum of the source was needed, the local oscillator had to be swept in frequency and the single pixel back end provided the spectrum. If a single channel map were desired, the local oscillator was fixed and the telescope swept over the desired area of the sky. [▶ Figure 7-9](#) shows a photograph of the InSb receiver mounted at the focus of the NASA Kuiper Observatory, used for frequencies from 400 to 600 GHz.

A superconducting version of the hot electron bolometer has been developed more recently (Gershenson et al. 1990). This is a device in which a small area (submicron) of a thin superconducting ribbon (a few nm) is heated by the DC bias and the local oscillator power (McGrath et al. 1997) and the IF passband is determined by the phonon interactions which cool the electrons (see [▶ Fig. 7-10](#)). An alternative mixer has been constructed using the electron diffusion out of the hot region to provide the cooling (Prober 1993) (see [▶ Fig. 7-11](#)). Both styles of HEB have fast electron cooling which allows an IF of about 2 GHz. The superconducting material is



■ Fig. 7-8

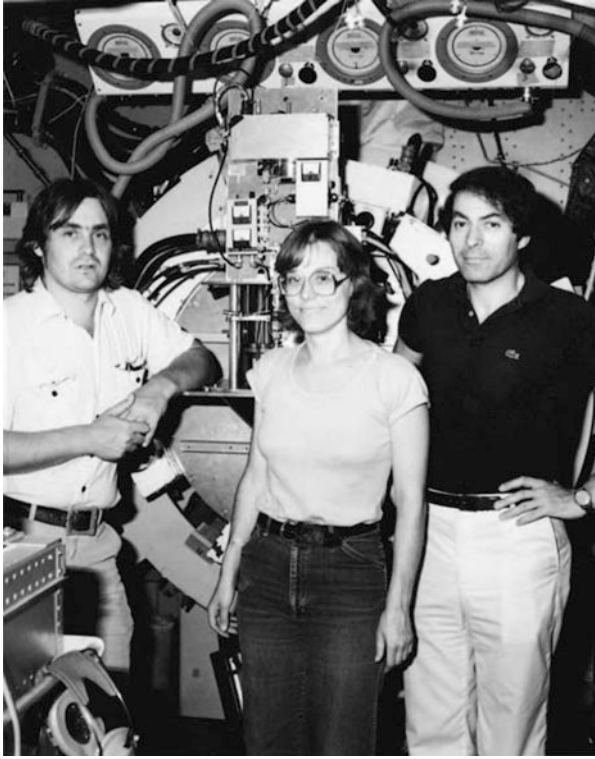
The waveguide mount for the InSb hot electron bolometer. The device is matched to the waveguide by an E-H tuner and a backshort

either Nb or NbN. The upper end of the frequency response of the devices is determined by the available local oscillator power. Probably the most effective application, to date, is in the HIFI instrument on Herschel where the local oscillator power is available to 1.9 THz. This is achieved by means of a synthesizer at ~ 30 GHz which is multiplied up by a series of multipliers (Pearson et al. 2000).

2.1.2 SIS Detectors

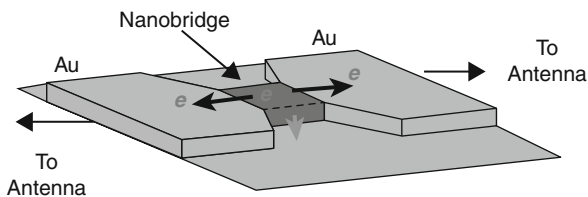
Superconductor-insulator-superconductor (SIS) receivers were developed independently at Bell Labs for 115 GHz mixing (Dolan et al. 1979) and for 36 GHz (Richards et al. 1979) at Berkeley. They have proved to be the most effective receivers in the submillimeter band of 100–800 GHz and have been used in nearly all receivers in telescopes which work in this range. Although considerable success had been achieved by the semiconductor hot electron bolometer receiver in opening up a new, complex, and interesting field, it was clear that a better receiver was needed as the 1-MHz baseband was unacceptable for a general purpose instrument. The alternative at that time was to attempt to operate the Schottky diode receivers at submillimeter wavelengths. Although this was possible, they were rather noisy, so an improved low-temperature receiver was required. The low-temperature solution to the receiver problem came about from the intense rivalry between AT&T and IBM in their competition to develop a superconducting computer. Neither company was successful, mainly due to the instability of the lead alloy superconducting tunnel junction electrodes. However, they did develop a high-frequency switching system using superconducting tunnel junctions which could be used as fast millimeter or submillimeter wave detectors. Bell Labs supported this and the necessary lithography.

The effect in use is the photon-assisted quasiparticle tunneling discovered by Dayem and Martin at Bell Labs (1962), but passed over as a device due to the more glamorous Josephson



■ Fig. 7-9

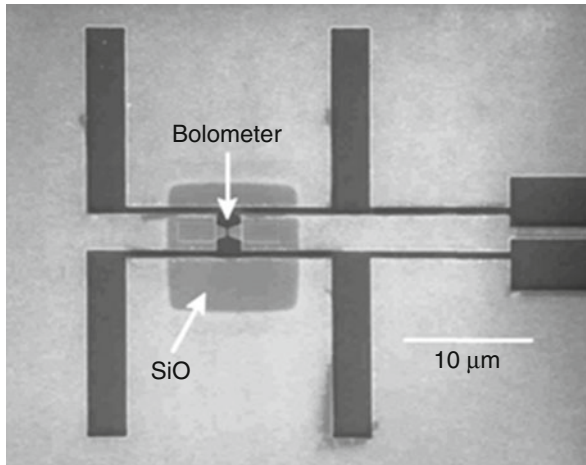
From the left: Chas Beichman, Jocelyn Keene, and Tom Phillips with the InSb receiver mounted at the focus of the 91.5-cm telescope of the Kuiper Airborne Observatory (KAO), operated by NASA



■ Fig. 7-10

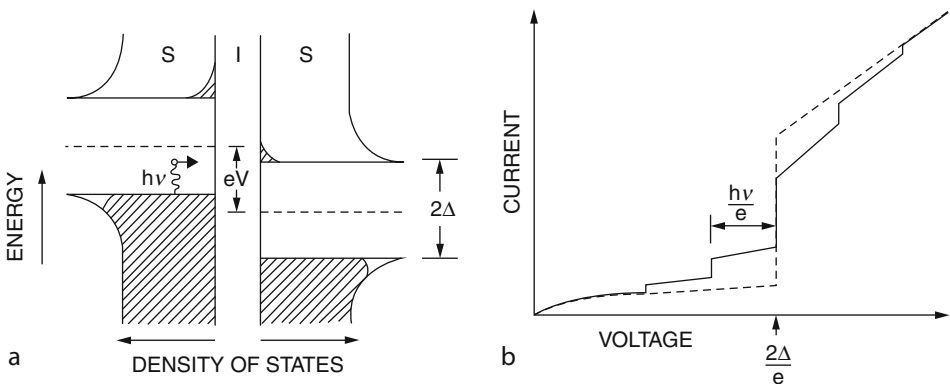
Basic geometry of the superconducting HEB mixer device

junction discovered soon afterward which, however, eventually proved too noisy. The physics of this low-temperature, quasiparticle tunneling superconducting device is related to that of the photodetectors used in the optical and infrared where the bandgap of semiconducting materials of about 1 eV is suitable to allow absorption of optical/IR photons. Equivalently, the superconducting energy gap of typically 1 or 2 meV is suitable for photo-detection in the millimeter and submillimeter involving the breaking of Cooper pairs. The superconducting devices are now known by their structure, “superconductor-insulator-superconductor” (SIS), rather



■ Fig. 7-11

SEM of Nb HEB mixer-embedding circuit showing twin-slot antenna and CPW lines. Inset shows area around the submicron device



■ Fig. 7-12

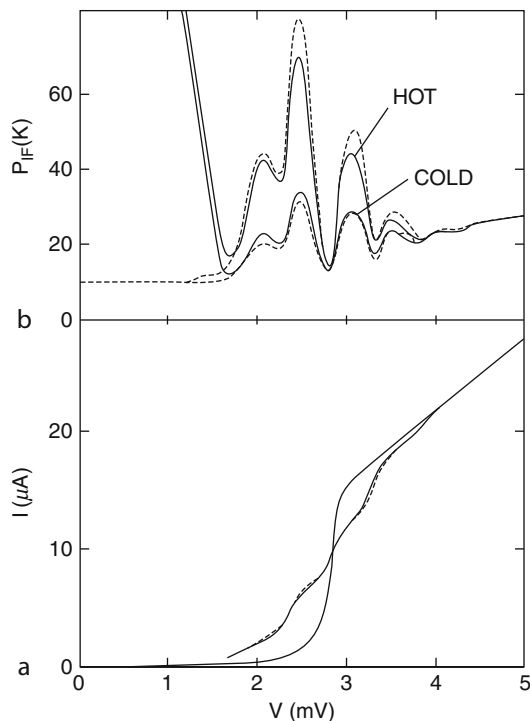
(a) Diagram of the superconducting bandgap and photon-assisted tunneling. (b) Idealized current as a function of the voltage. *Dotted line* is without any radiation and the *solid line* is with local oscillator radiation applied

than their physics since the SIS structure supports both quasiparticle and Josephson tunneling. This device, using the lead alloy materials, was mounted on a telescope for the first time in 1979 (Phillips and Woody 1982). The lead alloy materials were notoriously unstable both chemically and physically and were eventually replaced by niobium which is acceptably stable. During this time, an excellent theory of the operation of the SIS detector was developed by John Tucker (1979).

Early work on quasi-particle tunneling at Bell Labs demonstrated photon assisted tunneling which is revealed by step structure in the current vs. voltage at a spacing of $h\nu/e$ when local oscillator (LO) radiation at a frequency ν is applied (Dayem and Martin 1962). ➤ [Figure 7-12](#)

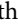
shows a diagram of the superconducting bandgap and photon-assisted tunneling for an SIS junction along with an idealized current vs. voltage characteristic. The quasiparticle tunneling description predicted the current vs. voltage characteristics as a function of the LO drive level, and this in turn was used to develop a phenomenological prediction of the mixer conversion efficiency (Phillips and Woody 1982).

The steps in the current vs. voltage relationship were seen in the early mixers and are shown in [Fig. 7-13](#) for an SIS receiver operating at 115 GHz. The hot and cold response does not look impressive by today's standards but achieving even this performance for the first-generation devices demonstrated the excellent potential for SIS mixers at millimeter and submillimeter wavelengths. A critical issue for SIS mixers was verification that it was the quasiparticle tunneling and not Josephson-pair tunneling that was responsible for the IF output power. A magnetic field is very effective at suppressing the effects of Josephson-pair tunneling. As seen in [Fig. 7-13](#), the IF output power near 0 v was decreased dramatically when a magnetic field was applied, but the output power at the photon step at the 2.3-mV gap voltage was only slightly changed by the application of a magnetic field. The conversion efficiency and noise temperature



■ Fig. 7-13

(a) Current vs. voltage characteristic without and with 115 GHz LO applied. (b) IF output power with the receiver looking at a 300 K room temperature load and at a 77 K liquid nitrogen load with the LO on. The solid line is without any magnetic field applied and dashed line is with a magnetic field applied. The photon-assisted tunneling is clearly revealed by the modulation in IF power as a function of the bias voltage (Woody 2009)

actually improved with the application of the magnetic field.  [Figure 7-12](#) also shows that even at 115 GHz the voltage step size is a significant fraction of the superconducting bandgap voltage. As these devices were pushed to higher frequencies, the Josephson-pair tunneling became more troubling, and new alloy systems needed to be developed for THz receivers.

Tucker's development of the full quantum mechanical description of quasi-particle tunneling and mixing in SIS tunnel junctions was a major advance that enabled a complete description and prediction of both the conversion efficiency and noise (Tucker 1979). This theory showed that the performance of SIS heterodyne mixers is limited only by the added noise imposed by quantum mechanics (Caves 1982; Wengler and Woody 1987). The mixers have conversion gains greater than unity, exceeding the limits for classical heterodyne mixing. This theoretical work was quickly incorporated into the receiver design process resulting in well-engineered astronomical receivers. Receiver performance within a factor of a few of the quantum limit for heterodyne mixing became feasible.

The critical component in SIS receivers is the tunnel junction. The current density, area, gap voltage, leakage current, as well as the stability of the thin film materials used are all important for producing reliable astronomical SIS receivers with good performance.


The widespread adoption of the SIS receivers on radio telescopes required the development of more reliable thin film systems. Most SIS receivers in the millimeter and low-frequency submillimeter band now utilize devices with Nb electrodes and Al-oxide tunnel barriers. This system produced high-quality devices with predictable and stable design parameters with the tuning structures and matching circuits fabricated on the chips along with the SIS device. Excellent performance is achieved throughout the millimeter and submillimeter bands (Kooi et al. 1992).

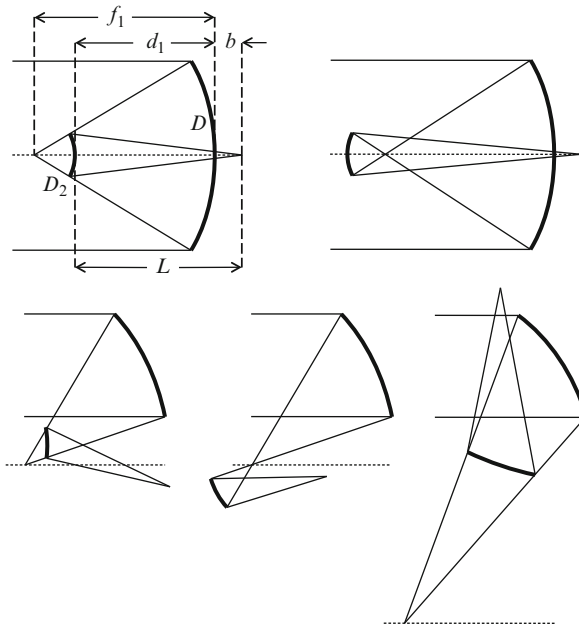
3 Telescopes

3.1 Optics

Most submillimeter telescopes are two-mirror reflecting telescopes (Baars 2007; Korsch 1991) similar to those used at optical and IR wavelengths (Wilson 1996, 1999). Reflecting surfaces have low loss, and the folded optical path results in a compact design, which is an important advantage for the telescope structure. The following sections give an overview of the most common designs. The emphasis here is on ground-based telescopes, but some examples of space telescopes are included.

3.1.1 Cassegrain and Gregory Telescopes

Submillimeter telescopes are usually on-axis Cassegrain or Gregory designs. Optical layouts for these telescopes are shown in  [Fig. 7-14](#). The classical Cassegrain and Gregory forms both have a paraboloidal primary (conic constant $b_1 = -1$). In the Cassegrain form, a convex hyperboloidal secondary (conic constant $b_2 < -1$) relays the inaccessible image at prime focus to the Cassegrain focus, which is usually behind the primary. A flat tertiary is often included to provide a Nasmyth focus on the elevation axis. The Cassegrain is the shortest of the two-mirror designs, so it is widely used. Examples of submillimeter classical Cassegrain telescopes include



■ Fig. 7-14

Cassegrain (top left) and Gregory (top right) telescopes, their off-axis variants (bottom left and center), and the crossed Mizuguchi-Dragone (bottom right). The horizontal dotted line in each diagram is the optical axis of the primary. D and D_2 are the diameters of the primary and secondary mirrors

CSO, JCMT, SMA, SMT, IRAM, APEX, ALMA, and Herschel (see ► Table 7-1). In the Gregory form, the secondary is a concave ellipsoid (conic constant $-1 < b_2 < 0$), mounted just beyond prime focus. The Gregory is longer, but its concave secondary is easier to test.

Submillimeter telescopes usually have a fast primary to keep the secondary support structure small. A primary focal ratio ≤ 0.4 minimizes the size and cost of the enclosure because the volume swept out by the telescope is set by the telescope diameter. Given the primary focal length, f_1 , and a back focal distance, b , chosen to give reasonable access to instruments, the focal length of the telescope, f , or secondary magnification, $m_2 = f/f_1$, or secondary diameter, D_2 , fixes the design (Wilson 1996). Small blockage generally requires $D_2 < D/10$, but if D_2 is too small, the focal length of the telescope becomes unreasonably large. The layout is specified by the secondary to image separation

$$L = |f| \frac{D_2}{D} = f \frac{1 - b/f_1}{1 - m_2}, \quad (7.1)$$

and the primary to secondary separation

$$d_1 = b - L = f_1 \frac{b/f_1 - m_2}{1 - m_2}, \quad (7.2)$$

and the secondary surface is specified by its radius of curvature

$$r_2 = \frac{2L}{1 + m_2}, \quad (7.3)$$

Table 7-1
Submillimeter telescopes^a

Telescope	Location	Altitude m	Diameter m	Surface error $\mu\text{m rms}$	Configuration ^b	Segments and support ^c	Enclosure
CSO (Leighton 1978)	Hawaii	4,200	10.4	13	Cassegrain	Al/Ah/Al, steel truss	Al dome, vertical shutter
JCMT (Baars 2007)	"	4,200	15	24	"	Al/Ah/Al, steel truss	Cylinder, sliding doors
SMA (Blundell 2007)	"	4,200	8 × 6	13	"	mAl, CFRP truss	No
SMT (HHT) (Baars 2007)	Arizona	3,300	10	15	"	CFRP/Ah/CFRP, CFRP truss	Box, hinged doors
IRAM (Baars et al. 1994; Guilloleau et al. 1992; Morris et al. 2009)	Spain	2,850	30	50	"	Al/Ah/Al, steel truss	No
	France	2,550	6 × 15	61	"	CFRP/Ah/CFRP, steel/CFRP truss	No
ALMA (Mangum et al. 2006; Saito 2011)	Chile	5,100	54 × 12	25	"	mAl, CFRP/Ah/CFRP box	No
APEX (Gusten et al. 2006)	"	5,100	12 × 7	20	"	eNi/Ah/eNi, CFRP plates mAl, steel truss	No
NANTEN2	"	4,900	4	17	"	"	No
KOSMA ^d (Kramer et al. 1998)	Switzerland	3,100	3	20	"	mAl, CFRP	Dome, horizontal shutter
AST/RO ^e (Stark, et al. 2001)	South Pole	2,800	1.7	30	OAG	mAl, CFRP truss	Dome, horizontal shutter
SPT (Carlstrom et al. 2011)	"	2,800	10	9	"	CFRP	Cloth dome, clamshell
ACT (Fowler et al. 2007; Swetz et al. 2011)	Chile	2,800	6	20	"	mAl, CFRP box	No
WMAP (Page et al. 2003)	L2	5,190	0.7	31	"	mAl, Al	Ground shield
Planck (Tauber et al. 2010)	L2		1.5	76	"	CFRP/KOREX/CFRP	
Herschel (Pilbratt et al. 2010)	L2		3.5	50	"	CFRP	
				2.5	Cassegrain	SIC	

^aThis list also includes some millimeter-wave telescopes to illustrate design options with low blockage

^bOAG = off-axis Gregory

^cAl/Ah/Al indicates a segment with Al facesheets and an Al honeycomb core. mAl/ machined Al, eNi electroformed Ni

^dMoved to Tibet in 2010

^eDecommissioned in 2005

■ Table 7-2

Sign conventions

Sign	Cassegrain	Gregory
+ve	f, b, L	b, L, m_2
-ve	f_1, d_1, m_2	f, f_1, d_1

■ Table 7-3

Third order aberrations for classical Cassegrain and Gregory telescopes (Schroeder 2000).

Aberration	Angular spot size ^a	FOV/ (λ/D)
Sagittal coma	$\theta/16F^2$	$32F^2$
Astigmatism	$\theta^2/2F_1$	$2(2F_1D/\lambda)^{1/2}$
Field curvature ^b	θ^2D/r_2	$2(r_2/\lambda)^{1/2}$

^a θ is the field angle, $F = f/D$ is the final focal ratio, $F_1 = f_1/D$ is the primary focal ratio, and r_2 is the radius of curvature of the secondary mirror. The terms for astigmatism and field curvature assume small back focal distance and large secondary magnification, which is typical for submillimeter telescopes. The Cassegrain and Gregory designs have the same coma and the same astigmatism

^b For the Cassegrain design, the focal surface is concave viewed from the secondary. For the Gregory, the focal surface is convex

and conic constant

$$b_2 = - \left(\frac{m_2 - 1}{m_2 + 1} \right)^2. \quad (7.4)$$

Sign conventions for (● 7.1–7.4) are shown in (● Table 7-2).

(● Table 7-3) shows aberrations for classical Cassegrain and Gregory telescopes. A submillimeter telescope typically has a primary focal ratio ≤ 0.7 , so field curvature and astigmatism are the largest aberrations. Field curvature can be corrected by a field-flattening lens, or by tiling the detectors on a faceted approximation to the focal surface, so astigmatism limits the FOV. It is difficult to make fast mirrors for optical wavelengths, so optical telescopes typically have a primary focal ratio in the range 1–2, and coma becomes more important. Third order coma can be eliminated by changing the conic constants of the primary and secondary to

$$b'_1 = -1 - \frac{2L}{d_1 m_2^3}$$

$$b'_2 = - \frac{2f}{d_1 (m_2 + 1)^3} - \left(\frac{m_2 - 1}{m_2 + 1} \right)^2, \quad (7.5)$$

resulting in the RC and aplanatic Gregory designs. The absence of coma and short overall length makes the RC form the choice for most optical and IR telescopes. Adjusting the conic constants of the primary and secondary does mean that the optical configuration is fixed, so it is not possible to change the final focal length by installing a new secondary, as is the case for the classical forms. The hyperboloidal RC primary also renders prime focus useless without a corrector. Since third-order coma does not limit the FOV in a telescope with a fast primary, all existing submillimeter telescopes are classical Cassegrain and Gregory designs. However, the development of large submillimeter detector arrays is pushing new telescopes to much wider FOV, which requires optical designs with good correction of higher order aberrations. As an example, the 25-m-diameter CCAT is a RC design with a shaped tertiary. This gives 0.9° FOV at $\lambda = 350 \mu\text{m}$, compared with 0.7° for a similar classical design with a shaped tertiary.

If the blockage due to the secondary and its support cannot be tolerated, an off-axis design must be used. This is often the case at longer wavelengths, where scattering from the telescope would exceed the loss through the atmosphere, or for observations of low surface brightness extended sources where false signals due to scattering and sidelobes would be a problem. The Gregory form is generally used for wide-field, off-axis designs because it gives a less offset primary and easy access to a pupil for chopping and scanning. Off-axis optical systems suffer from severe astigmatism and coma, but the secondary can be tilted to correct astigmatism (Dragone 1978, 1982; Hanany and Marrone 2002; Rusch et al. 1990), and the mirrors can be shaped to reduce coma, resulting in a FOV similar to that of an on-axis design with the same primary diameter and focal length. The secondary must be tilted to satisfy

$$m'_2 \tan i_1 = (m'_2 + 1) \tan i_2, \quad (7.6)$$

where m'_2 is the magnification of the tilted secondary and i_1 and i_2 are the angles of incidence of the principal ray at the primary and secondary. Examples of off-axis Gregory telescopes include AST/RO, SPT, ACT, WMAP, and Planck. With the exception of AST/RO, these are all millimeter-wave telescopes designed for CMB observations.

Most submillimeter instruments have a cold stop to control the illumination on the primary, so the entrance pupil is a little smaller than the primary mirror. In some cases, the stop can be at the secondary mirror, with the spillover falling on the cold sky, or on a cooled absorber (Padin et al. 2008a).

The main disadvantage of the Cassegrain and Gregory designs is the tight alignment tolerance. Most submillimeter telescopes provide active control of the secondary position to compensate gravitational deflection of the secondary support.

3.1.2 Plate Scale

In on-axis designs, the Cassegrain or Gregory focus is usually placed just behind the primary, partly to avoid blockage due to placing a large camera in the telescope beam and partly to give easy access to the camera. This configuration requires a telescope focal ratio greater than $\sim f/5$, which may lead to unreasonably large detectors. Submillimeter telescopes generally have a focal reducer to couple the telescope to the detectors.

For maximum aperture efficiency, a detector should just fill the central part of the Airy pattern delivered by the telescope, so the detector diameter must be $2F\lambda$, where F is the focal ratio at the detector. Arrays of $2F\lambda$ feedhorn-coupled detectors are often used for small cameras. The telescope FWHM beamwidth corresponds to $F\lambda$ at the detectors, so a detector array that Nyquist samples the sky must have $0.5F\lambda$ detectors. If the number of detectors is limited, e.g., by cost, $2F\lambda$ detectors give the highest mapping speed; otherwise, smaller pixels are better (Griffin et al. 2002). The typical size of an absorber-coupled submillimeter detector is 1 mm, so a $0.5F\lambda$ detector must be fed at $\sim f/3$. This usually requires a focal reducer, which can be a single off-axis ellipsoid for small FOV (Serabyn 1997). A focal reducer for larger FOV might use a pair of off-axis ellipsoids with an intermediate focus. Aberrations from the first off-axis ellipsoid can be at least partly compensated by the second (Serabyn 1995).

In an off-axis telescope, the camera can be placed in front of the primary without blocking the beam. In this case, the telescope focal ratio can be made small enough to directly feed the detectors, leading to a very simple, low-loss optical system (Padin et al. 2008a). The main

disadvantage of such an approach is that the camera must be mounted close to the secondary mirror, so access is difficult and the camera moves around as the telescope tracks and scans.

3.1.3 Other Telescope Designs

Cassegrain and Gregory designs dominate at submillimeter wavelengths, but other designs are sometimes used. The crossed Mizuguchi-Dragone telescope is an off-axis design with a large secondary (see [Fig. 7-14](#)). It offers significantly wider FOV and better polarization performance compared with an off-axis Gregory of the same size (Dragone 1983; Tran et al. 2008). The crossed design has been proposed for CMB observations that do not require a large telescope. Refracting telescopes have been built for similar applications (Keating et al. 2003). Refracting optics are widely used inside submillimeter cameras and spectrometers, but dielectrics are quite lossy at submillimeter wavelengths, so thick lenses must be cooled. This severely limits the size of a refracting telescope.

3.1.4 Chopping and Scanning

Cassegrain telescopes are often equipped with a chopping secondary which allows a small field to be switched rapidly between the source and a reference position. Differencing the on and off source positions removes offsets and fluctuations in sky brightness (due to variations in the water vapor column) on timescales longer than the switching period. Chopping is an important technique for ground-based spectroscopy because sky brightness fluctuations typically dominate the noise. The throw for a chopping secondary is usually of order 10 beamwidths, limited by aberrations due to the tilt of the secondary. The chopping period must be a few times smaller than the wind crossing time, which is ~ 1 s for a 10-m telescope with a typical 10 ms^{-1} wind speed (Radford et al. 2008). Fast chopping with a large secondary is challenging, so chopping secondary mirrors are often made of very lightweight materials, e.g., CFRP or beryllium.

In an off-axis Gregory telescope, the pupil just after the secondary is a convenient, accessible location for a chopping mirror. In this case, the chopping mirror is a flat that can be tilted to generate a phase gradient across the pupil, which is equivalent to shifting the telescope beam on the sky. Chopping at a pupil allows a large chop throw without degrading the image quality over a wide FOV. Examples of telescopes with chopping flats include AST/RO and the Viper millimeter-wave telescope (Peterson et al. 2000). The development of large detector arrays has significantly reduced the requirements for chopping because sky brightness fluctuations are correlated across the detector array, so much of the sky signal can be removed by subtracting the average over the array (Jenness et al. 1998; Sayers et al. 2010).

For imaging observations, the telescope beam is usually scanned in a pattern that gives uniform coverage across the source, e.g., a raster or Lissajous pattern. Scanning fully samples the source, and allows the removal of offsets and sky brightness fluctuations that appear as low-frequency variations in the detector timestreams. During a scanning observation, it is usually sufficient for the telescope to follow the commanded path within about $1/2$ a beamwidth to maintain adequate coverage. The actual path is then accurately reconstructed after the observation using encoder readings and models of the telescope deformation due to acceleration. A scanning flat at a pupil can be used to scan the beam, and may be appropriate if very fast scanning is needed, but now it is often possible to scan the entire telescope at speeds of

order 1° s^{-1} . The SPT and ACT millimeter-wave CMB experiments, which are both Gregory designs, scan the entire telescope rather than a flat at a pupil. The major disadvantage of scanning the entire telescope is mechanical noise, which can cause problems for refrigerators and high-impedance detector readouts.

3.1.5 Scattering and Loss

Scattering and loss in the telescope degrade the aperture efficiency, increase the loading on the detectors, and may cause false signals. The main scattering contributions are blockage due to the secondary (typically 1% in an on-axis telescope), the secondary support (a few percent) (Cheng and Mangum 1998; Lamb and Olver 1986), gaps between mirror segments (usually $<1\%$), and surfaces of refractive elements inside cameras and spectrometers. Some of the scattering from the telescope can be directed to the sky, e.g., by using shaped secondary support legs (Lawrence et al. 1994; Moreira et al. 1996) and covering segment gaps with reflecting strips (Padin et al. 2008b), but some of the scattered light will be absorbed at ambient temperature.

On-axis telescope designs are generally adequate for ground-based observations at $\lambda < 1 \text{ mm}$ because the atmospheric transmission is worse than the telescope transmission. At longer wavelengths, the atmosphere is more transparent, so blockage is more important. This is one of the reasons millimeter-wave CMB experiments favor off-axis telescopes.

3.1.6 Optical Components

Primary mirrors for large telescopes must be segmented. Segments for submillimeter telescopes are made from machined Al (e.g., ALMA Vertex), electroformed Ni facesheets with an Al honeycomb core (e.g., ALMA Alcatel), Al facesheets with an Al honeycomb core (e.g., CSO), and aluminized CFRP with an Al honeycomb core (e.g., SMT). Conventional milling can achieve surface errors of $\sim 2 \mu\text{m}$ rms on a 0.5-m Al segment. The reflectivity of a machined Al mirror is $\sim 1 - 0.06 \times \exp(-\lambda/200 \mu\text{m})$ (Baars et al. 2006). Metal mirrors are too heavy for space telescopes, so CFRP facesheets with a CFRP core (e.g., Planck) or lightweighted SiC (e.g., Herschel) are used. These technologies are generally too expensive for ground-based telescopes.

The mass of the primary must be minimized because it is a strong driver for the overall mass and cost of a telescope. Machined Al segments can achieve an areal density of $\sim 20 \text{ kg m}^{-2}$, which is about the same as the areal density of the entire Herschel primary. The choice of segment size is a trade-off between manufacturing errors and thermal deformations, which increase with segment size, vs. areal density, complexity, and noise for active control, all of which decrease with segment size. Most submillimeter telescopes have 1–2-m segments.

Plastics are widely used for submillimeter lenses and windows, with machined grooves (Goldsmith 1998) or plastic foam anti-reflection (AR) coatings (Savini and Hargrave 2010). HDPE and UHMWPE (refractive index $n = 1.5$, loss tangent $\tan \delta \sim 5 \times 10^{-4}$ at $\lambda = 350 \mu\text{m}$) are popular because they have low loss in the submillimeter, but other plastics, e.g., teflon, nylon, and polystyrene, are used, particularly at longer wavelengths (Lamb 1996). High-resistivity Si ($n = 3.42$, $\tan \delta \sim 10^{-5}$ at $\lambda = 1 \text{ mm}$) has lower loss, and the high-refractive index generally gives better image quality, but AR coating is more difficult. AR coatings can be etched on small Si optics and polyimide (Fowler et al. 2007) layers have been used on larger Si lenses.

3.2 Structure and Mechanics

Structural and mechanical systems support the optical surfaces as the telescope scans and tracks a source. The quality of the wavefront delivered to the detectors is generally determined by the telescope structure, so this is a critical aspect of the telescope design. The following sections describe the key telescope systems and some simple models that illustrate typical performance at submillimeter wavelengths.

3.2.1 Pointing and Wavefront Errors

The telescope mount usually determines the pointing error, while the primary mirror support determines the mirror surface error and hence higher-order wavefront errors. All these errors are related in that a pointing error is just a tilt, which is the lowest-order wavefront error. It is usual to carry pointing and surface error as separate terms in the telescope error budget because the pointing error can easily be measured and corrected by observing a nearby, bright, point source. At submillimeter wavelengths, atmospheric seeing does not dominate the wavefront error under good observing conditions, so the telescope sees a diffraction-limited image (with resolution $1.22\lambda/D$) that moves around slowly as the telescope pointing error varies (typically $1\text{--}2''$ on timescales of hours).

3.2.2 Primary Mirror Support

The primary mirror is the most difficult part of any reflecting telescope. The key design consideration is maintaining the mirror surface accuracy in the presence of gravity, temperature variations, wind, solar illumination, and acceleration due to scanning. Gravitational and thermal deformations are the biggest problems for ground-based telescopes.

Telescope primary mirrors are essentially plate structures, so a simple model of the sag of a plate supported around its edge can provide some insight. The p-p deflection of a simply supported plate is (Timoshenko and Woinowsky-Krieger 1959)

$$\delta \approx \frac{qD^4}{24E\eta h^3}, \quad (7.7)$$

where q is the pressure on the plate, h is the plate thickness, E is Young's modulus for the plate material, and η is the filling factor. The pressure on the plate due to its own weight and the weight of the segments is

$$q \sim 2gh\rho\eta, \quad (7.8)$$

where g is the acceleration due to gravity and ρ is the density of the plate material. The factor 2 in (7.8) is a somewhat pessimistic estimate of the areal density of the segments. The thickness of a submillimeter primary mirror is typically similar to the depth of the primary surface, which is $D/8$ for a focal ratio of 0.5, so the rms gravitational deflection is

$$\sigma \approx \frac{\delta}{3} \sim \frac{2g\rho D^2}{E}, \quad (7.9)$$

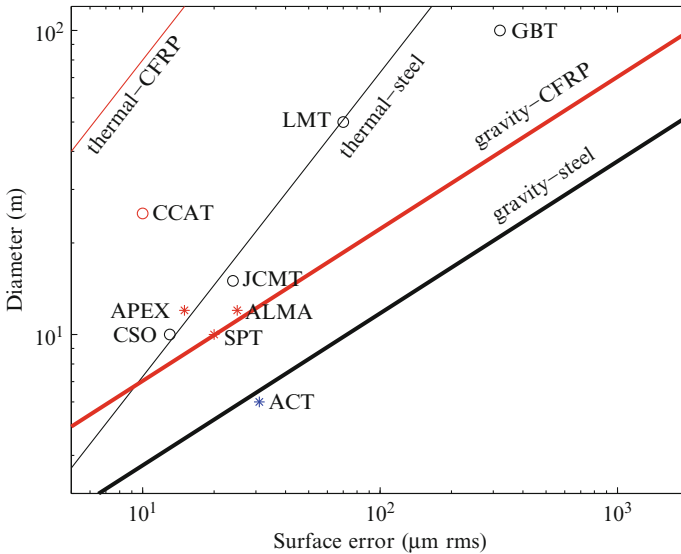


Fig. 7-15

Diameter vs. surface error for passive (*) and active (o) primary mirror supports made of steel (black), CFRP (red), and aluminum (blue). Points for CCAT and LMT are predictions. Materials properties are given in Table 7-4

where the rms is taken to be one third of the p-p. Temperature variations across the plate change its thickness, resulting in rms surface error

$$\sigma_T \approx \alpha T (D/8), \quad (7.10)$$

where T is the rms temperature variation and α is the coefficient of thermal expansion of the plate material. Equations 7.9 and 7.10 are plotted in Fig. 7-15 for different materials and 1-K-rms temperature variation, which is typical for a submillimeter telescope (Greve and Bremer 2010). The primary diameter vs. surface error plot is often called a von Hoerner plot after its inventor (von Hoerner 1967). The plot is useful because it indicates which materials must be used to achieve a given performance with a passive support structure, or alternatively when active control of the optical surfaces is needed. Passive supports are often designed to deform under gravity in a way that maintains a paraboloidal surface, but with an elevation-dependent focal length. These homologous designs achieve gravitational deflections a few times smaller than predicted by 7.9. The CSO uses a combination of homology and slow active control to beat the limits for gravitational deflection of its steel structure, so the performance is limited by thermal deformations. The GBT and LMT are examples of much larger, lower-frequency, telescopes with steel structures and fast active surfaces (Baars 2007). ALMA uses a CFRP structure to achieve the required performance with a completely passive support. ACT is made of Al, so its performance is limited by thermal deformations.

For a given surface error in **Fig. 7-15**, the Strehl ratio is

$$S = \exp - \left(\frac{4\pi\sigma}{\lambda} \right)^2, \quad (7.11)$$

which is the Ruze formula familiar to designers of microwave telescopes (Ruze 1966). High Strehl ratio places stringent demands on the surface error. For example, $S > 0.9$, corresponding to <20% increase in integration time compared with an ideal telescope, requires $\sigma < \lambda/39$, which is challenging at short wavelengths.

During a scanning observation, acceleration of the telescope causes the primary to deflect, resulting in pointing errors that can degrade the image resolution. The effect is small for existing submillimeter telescopes, which have large beamwidths and slow drives, but it will be important for future, large, submillimeter telescopes that scan quickly. The pointing error can be calculated in terms of the gravitational deflection or natural frequency, leading to some useful expressions that capture the dynamic performance of the primary. The stiffness of the primary is

$$k = \frac{mg}{\delta}, \quad (7.12)$$

where m is the mass of the primary, so the natural frequency is

$$\omega = \sqrt{\frac{k}{m}} = \sqrt{\frac{g}{\delta}} \sim \frac{1}{D} \sqrt{\frac{E}{6\rho}}. \quad (7.13)$$

The deflection of the primary due to angular acceleration Ω is

$$\delta_a \approx \Omega (D/4) \delta / g \approx \Omega (D/4) / \omega^2, \quad (7.14)$$

and the corresponding pointing error is

$$\theta_a \approx \delta_a / (D/4) \approx \Omega / \omega^2. \quad (7.15)$$

A 25-m primary made of steel should achieve ~14-Hz natural frequency, so at 1° s^{-2} acceleration, the pointing error should be $0.47''$, which is 1/7 of the beamwidth at $\lambda = 350 \mu\text{m}$, essentially the entire pointing budget. If the natural frequency were only 7 Hz, which is probably more realistic, the pointing error would be $>1/2$ the beamwidth, which is enough to severely degrade the image resolution.

Submillimeter telescopes often have a simple enclosure to protect the telescope from wind buffeting, solar heating, and severe weather (see **Table 7-1**). Wind protection is important for telescopes with light structures because these designs tend to have low stiffness, even though the stiffness to mass ratio is high enough to give small gravitational deformation. The rms wind-induced deformation of the primary is

$$\sigma_w \approx \sigma \frac{q_w}{q}, \quad (7.16)$$

where

$$q_w = \frac{1}{2} \rho_{\text{air}} v^2 \quad (7.17)$$

is the wind pressure, $\rho_{\text{air}} \approx 1 \text{ kg m}^{-3}$ is the density of air, and v is the wind speed. Combining **(7.16)**, **(7.13)**, **(7.9)**, and **(7.8)** yields

$$\sigma_w \sim \frac{1}{2} \rho_{\text{air}} v^2 \frac{8D}{E\eta} \sim \frac{1}{2} \rho_{\text{air}} v^2 \frac{1}{\omega^2 D \rho \eta}. \quad (7.18)$$

The outside wind speed at a submillimeter site might be 10 ms^{-1} , so $q_w \approx 50 \text{ Pa}$. For a 25 m diameter steel primary with 7 Hz natural frequency and 1% filling factor, this wind pressure will cause $\sim 13 \text{ }\mu\text{m}$ rms deformation, which is the entire surface error budget for a $\lambda = 350 \text{ }\mu\text{m}$ telescope and an order of magnitude larger than the fraction of the budget that might typically be allocated to wind-induced deformation. If this primary were exposed, its stiffness would have to be increased by an order of magnitude. Stiffness scales roughly with filling factor, so the cost of the primary support would also increase by an order of magnitude. However, wind pressure scales with the square of the wind speed, so even a simple enclosure can make the wind pressure negligible. This approach can be much less expensive than making the structure stiff enough to resist outside wind forces.

3.2.3 Mirror Control

Most existing submillimeter telescopes have passive primary mirror support systems, which can achieve $\sim 15\text{-}\mu\text{m}$ -rms surface accuracy on a $\sim 10\text{-m}$ telescope. The CSO is an example of a submillimeter telescope with an active primary. Its segments are attached to a steel spaceframe truss with $\sim 100\text{-mm}$ -long steel rods that can be heated to give $\sim 10 \text{ }\mu\text{m}$ of length adjustment. This allows slow active control which has improved the surface error from 22 to $\sim 13 \text{ }\mu\text{m}$ rms (Leong et al. 2006; Woody et al. 1998). Future, larger telescopes will have larger gravitational deformations and will require fast active control.

The simplest approach to active control is open loop, based on look up tables for gravity and temperature. The GBT, LMT, JCMT, and CSO use this type of control. Open loop control requires a mirror support with good repeatability. In practice, open loop control is limited by the thermal stability of the mirror support because it is difficult to generate a thermal model that can predict deformations on small spatial scales.

Closed loop control is used on segmented optical telescopes and may be needed for future, large, submillimeter telescopes. The usual approach is to measure the relative piston and tilt of neighboring segments using edge sensors. These can be capacitive displacement sensors, as in the Keck telescopes (Nelson et al. 1985), inductive sensors, as in HET (Booth et al. 2003) and SALT (Menzius et al. 2010), or optical sensors, as proposed for CCAT (Woody 2011). Edge sensors have good sensitivity to deformations on the scale of a segment, but the sensitivity to low-order modes of the primary is poor because many sensor readings must be combined to measure a low-order deformation. This is not a big issue for an optical telescope, because a wavefront measurement on a bright star can quickly constrain the low-order modes, but it is a serious concern for a submillimeter telescope, where submillimeter wavefront measurements are slow and a suitable source is often not available. If the noise for a single sensor is e_s (in units of length) and the noise is uncorrelated between sensors, the noise for a measurement of the lowest-order mode of the primary is

$$e_u \sim e_s \sqrt{D/d}, \quad (7.19)$$

where d is the size of a segment and D/d is the number of sensors across the mode. The factor $\sqrt{D/d}$ in (7.19) is often called the error multiplier. For an optical telescope, the sensor noise is mainly electrical noise, but a submillimeter telescope is made of materials with higher and less uniform coefficient of thermal expansion, so thermal deformation of the sensor mounts dominates. A submillimeter mirror segment might have $e_s \sim 1 \text{ }\mu\text{m}$ rms, so sensor noise is a serious issue for a large telescope. The situation is even worse for deformations that are correlated

between segments, e.g., gravitational deformation and cupping of the segments due to a thermal gradient through the segments. In this case, the noise for a measurement of the lowest-order mode is

$$e_c \sim e_s D/d. \quad (7.20)$$

In principle, an edge sensor system with enough sensors can measure cupping of the segments, so it may be possible to correct the effect of segment deformations in a closed loop control system.

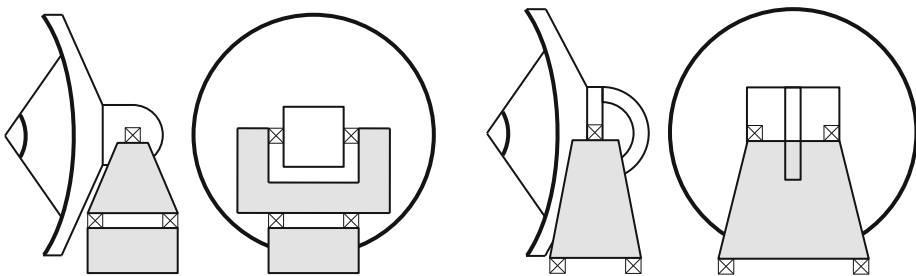
3.2.4 Telescope Mount

The telescope mount usually has little impact on the surface accuracy of the primary, but it does set the pointing performance. Most modern telescopes have an elevation over azimuth mount to minimize the mass and cost of the mount. There are many design variations, but elevation over azimuth mounts fall into two broad groups: a fork on a pedestal, or an alidade on a track (see [Fig. 7-16](#)). Mount structures are generally made of steel, to reduce the cost, and the filling factor for the structure is typically $\sim 1\%$ for box and spaceframe mount designs. The mounts in [Fig. 7-16](#) look roughly like beams $\sim D/2$ high $\times D/2$ wide (along the elevation axis) $\times D/4$ deep (fore-aft), so a simple beam model can provide a useful estimate of the performance. The stiffness of the beam for end loading is (Olberg et al. 1992)

$$k' \sim \frac{E' \eta' D}{64}, \quad (7.21)$$

where E' is Young's modulus for the mount material and η' is the filling factor. The primary requires a counterweight with mass similar to that of the primary, and an elevation axle that might be twice the mass of the primary, so the mass of the tipping structure is $\sim 4\times$ the mass of the primary. The mass of the mount is usually similar to the mass of the tipping structure, so the total mass of telescope is

$$m' \sim 16\pi (D/2)^2 (D/8) \eta \rho, \quad (7.22)$$



■ Fig. 7-16

Fork on pedestal (*left*) and alidade on track (*right*) telescope mounts. Crosses indicate bearings. Some fork mounts are inverted, with the fork arms attached to the primary rather than to the pedestal

where the mass of the primary is given by (7.8). The natural frequency of the telescope is then

$$\omega' \sim \sqrt{\frac{k'}{m'}} \sim \frac{1}{10D} \sqrt{\frac{E'\eta'}{\rho\eta}}. \quad (7.23)$$

For a steel structure, $\omega' / (2\pi) \sim 100/D$, where D is in meters. This is consistent with measured natural frequencies for radio telescopes in the 10–30-m-diameter range (Gawronski 2005).

Equation 7.23 is a rough but useful guide to the dynamic performance of the structure, and it immediately gives an estimate of the fast motion capabilities of the telescope because the drive control loop bandwidth must be a factor 4–10 smaller than the natural frequency. Thus, a 25-m steel telescope should achieve a drive bandwidth of 0.4–1 Hz, which would allow position switching at ~ 0.1 Hz. A CFRP primary would improve the drive bandwidth by roughly a factor 2.

A simple model can also give us a useful estimate of pointing errors due to temperature variations in the mount. For a massive structure like the mount, thermal deformations are mainly driven by diurnal temperature variations, while for lighter, open structures like the primary, spatial variations in air temperature are more important. The thermal time constant of the mount is

$$\tau = C/G, \quad (7.24)$$

where C is the specific heat and G is the thermal conductance. For pointing errors, we are concerned with temperature variations across the mount. Breaking the upper part of the mount into three slices, one for each elevation bearing and one in the center, gives

$$G \sim \beta (D/4)^2 \eta' / (D/6), \quad (7.25)$$

where β is the thermal conductivity of the mount material. The specific heat of one of the slices is

$$C \sim c (D/4)^2 (D/6) \eta' \rho', \quad (7.26)$$

where c and ρ' are the specific heat capacity and density of the mount material. The thermal time constant is then

$$\tau \sim \frac{c\rho'}{\beta} \times \frac{D^2}{36}. \quad (7.27)$$

For a steel mount, $\beta/c\rho' = 1.4 \times 10^{-5} \text{ m}^2 \text{ s}^{-1}$ (see Table 7-4), so $\tau \sim D^2/2 \text{ h}$, where D is in meters. If the mount acts as a single-pole, low-pass, thermal filter, the mount temperature is

Table 7-4
Material properties (Wilson 1999)

Property	Symbol	Units	Aluminum	Steel	CFRP
Density	ρ	kg m^{-3}	2,600	7,850	1,550
Young's modulus	E	Pa	7×10^{10}	2.1×10^{11}	1.5×10^{11}
Stiffness	E/ρ	J kg^{-1}	2.7×10^7	2.7×10^7	9.7×10^7
Coefficient of thermal expansion	α	K^{-1}	2.2×10^{-5}	1.1×10^{-5}	2×10^{-7} to 10^{-6}
Specific heat capacity	c	$\text{J kg}^{-1} \text{K}^{-1}$	890	460	
Thermal conductivity	β	$\text{W m}^{-1} \text{K}^{-1}$	160	49	
Thermal diffusivity	$\beta/(c\rho)$	$\text{m}^2 \text{s}^{-1}$	6.9×10^{-5}	1.4×10^{-5}	

$$T(t) \sim (\Delta T/\tau) \sin(2\pi t), \quad (7.28)$$

where ΔT is the amplitude of diurnal variations in air temperature. Temperature gradients across the mount can be as large as $T(t)$, in which case the pointing error is

$$\theta_T \sim \alpha' T(t), \quad (7.29)$$

where α' is the coefficient of thermal expansion of the mount material. Pointing errors are usually measured by observing a nearby bright point source, and the measurements are made often enough to keep the pointing error smaller than about 1/10 of the beamwidth. The time between pointing measurements is then

$$t' < (1/10) (1.22\lambda/D) / \dot{\theta}_T \sim \lambda D / (100\alpha' \Delta T) \text{ h}, \quad (7.30)$$

where D and λ are in meters. ΔT is typically 5 K at high desert sites (Radford et al. 2008), so for a 10-m steel telescope at $\lambda = 350 \mu\text{m}$, $t' < 3/4$ h. Pointing measurements typically take a few minutes, so a measurement roughly every hour does not significantly impact the observing efficiency. Since the thermal time constant scales with D^2 , larger telescopes have better mount thermal performance, despite the smaller beamwidth.

Telescope mounts are equipped with encoders to measure the position of the axes. Most modern telescopes use optical tape or disk encoders. A tiltmeter is often mounted on the azimuth axis to measure changes in the overall tilt of the structure. Some mounts include metrology systems to directly measure thermal deformations of the yoke, and some use temperature sensors to predict thermal deformations. All existing submillimeter telescope mounts have rolling element bearings, but hydrostatic bearings will likely be used on future, large, submillimeter telescopes. The drives are typically brushless DC motors with gearboxes driving a ring or sector gear, but some telescopes (e.g., ALMA, Mangum et al. 2006) have direct drives.

3.3 Alignment

The telescope optics must be aligned when the telescope is built, and alignment must be maintained during observations. This is a difficult problem. Some of the techniques that have been developed for aligning submillimeter telescopes are described below. These fall into two groups: direct measurements of the mirror surfaces and measurements of the wavefront delivered to a detector. In general, telescope alignment starts with direct measurements and then moves to wavefront measurements when the errors are much smaller than the observing wavelength.

Initial alignment of submillimeter telescope surfaces used to be done with a theodolite and tape, which can achieve a few $\times 100\text{-}\mu\text{m}$ -rms surface errors on a 10-m telescope, but photogrammetry and laser trackers are now widely used. Photogrammetry involves taking photographs of reflective targets on the primary from different angles. A calibrated ruler is included somewhere in the photographs to give the overall scale. Photogrammetry can measure features to about one part in 10^5 , i.e., a few $\times 10 \mu\text{m}$ rms for a 10-m primary. This technique was used for initial alignment of ALMA, and SPT. Laser trackers use precise measurements of the angle of a laser beam reflected from a retro-reflector on the surface being measured, combined with interferometry to measure the distance to the surface. The retro reflector is usually a corner cube mounted in a sphere that can be moved around on the surface. A laser tracker can measure features to a few $\times 10 \mu\text{m}$ rms on a 10-m primary in the field, but much more accurate results can be achieved

under controlled conditions (Zobrist et al. 2009). ACT was aligned using a laser tracker (Hincks et al. 2008).

Following initial alignment, millimeter-wave holography (Bennett et al. 1976; Scott and Ryle 1977) is often used to measure and correct the surface. Holography measurements can easily achieve an accuracy of a few microns. The technique measures the far field response of a telescope, which is the Fourier Transform of the complex illumination pattern on the primary. The phase of the illumination pattern corresponds to the wavefront error. A measurement of the far field response requires an interferometer in which the telescope under test is scanned across a source while the reference telescope is fixed on the source. A bright celestial source, e.g., a planet, can be used to measure the wavefront over a range of elevations. This type of measurement typically requires a large reference telescope, so it is easy for telescopes in an array, but rarely practical for a single telescope. An artificial source on a tower can be used (Baars et al. 2007), in which case the reference telescope might be just a small horn, but this measurement yields the near field response. The far field response can be calculated if the relative position of the source and telescope is known. For some near field holography measurements, the reference horn is mounted on the back of the secondary of the telescope being measured. In this case, the horn also moves, but it is small, so its response does not change much. The main problem with measurements that use an artificial source on a tower is that the surface can be measured at only one, low elevation.

Out of focus holography (Morris et al. 1991; Nikolic et al. 2007a) can be used to measure low-order wavefront errors because they change the shape of the PSF. The technique involves measuring the PSF at and on either side of focus, e.g., by moving the secondary while observing a bright point source with a camera. Model fits to the PSF yield the first few modes of the wavefront. This is useful because the largest errors are typically in the lowest-order modes. Out of focus holography is routinely used to measure and correct the 100-m diameter GBT (Nikolic et al. 2007b).

The CSO uses a shearing interferometer (Serabyn et al. 1991) to measure wavefront errors. This is another way of measuring the far field response of the telescope, but instead of using a reference telescope, as in holography, light from the core of an image of a point source provides the reference. The beam from the telescope is split and then recombined at a focus so that one point source image (the signal) can be moved relative the other (the reference). A path length modulator is included in the reference arm so that a total power detector can measure the complex field vs. frequency where the reference and signal images overlap. The signal image is stepped across the reference until the response function has been sampled to large enough radius to give the desired spatial resolution on the primary.

Phase contrast interferometry (Dicke 1975; Malacara 1992; Serabyn and Wallace 2010) is another promising technique for submillimeter wavefront measurements. In this case, a camera is used to inspect the pupil while the average phase of the illumination is changed. A $\pi/2$ phase shift converts small phase variations into brightness variations, so a measurement of the brightness over the pupil gives the wavefront error. The phase shift is done by modulating the path length at the core of a point source image, either using phase plates or a small moving mirror in the center of a larger mirror. CCAT will use phase contrast interferometry to set and maintain its optics. A measurement of the 25-m surface with 0.5-m spatial resolution and a few μm rms accuracy will take ~ 10 s on Mars to ~ 2 h on Uranus, depending on the wavelength (Serabyn 2006).

References

- Baars, J. W. M. 2007, *The Paraboloidal Reflector Antenna in Radio Astronomy and Communication* (New York: Springer)
- Baars, J. W. M., et al. 1994, *Proc. IEEE*, 82, 687–696
- Baars, J. W. M., et al. 2006, ALMA Memo 566 NRAO, Charlottesville VA
- Baars, J. W. M., et al. 2007, *IEEE Antennas Propag. Mag.*, 49, 24–41
- Bennett, J. C., et al. 1976, *IEEE Trans. Antennas Propag.* 24, 295–303
- Blake, G. A., Keene, J., & Phillips, T. G. 1985, Chlorine in dense interstellar clouds – the abundance of HCl in OMC-1. *ApJ*, 295, 501
- Blake, G. A., Sutton, E. C., Masson, C. R., & Phillips, T. G. 1987, Molecular abundances in OMC-1 – the chemical composition of interstellar molecular clouds and the influence of massive star formation. *ApJ*, 315, 621
- Blundell, R. 2007, in *IEEE/MTT-S International Microwave Symposium* (New York: IEEE), 1857–1860
- Booth, J. A., et al. 2003, *Proc. SPIE*, 4837, 919–933
- Carlstrom, J. E., et al. 2011, *PASP*, 123, 568–581
- Caves, C. 1982, Quantum limits on noise in linear amplifiers. *Phys. Rev. D*, 26, 1817
- Cheng, J., & Mangum, J. G. 1998, MMA Memo, Vol. 197 (Tucson: NRAO, Charlottesville VA)
- Dayem, A. H., & Martin, R. J. 1962, Quantum interaction of microwave radiation with tunneling between superconductors. *Phys. Rev. Lett.*, 8, 246
- Dicke, R. H. 1975, *ApJ*, 198, 605–615
- Dolan, G. J., Phillips, T. G., & Woody, D. P. 1979, Low-noise 115 GHz mixing in superconducting oxide-barrier tunnel junctions. *Appl. Phys. Lett.*, 34, 347
- Dragone, C. 1978, *Bell Syst. Tech. J.*, 57, 2663–2684
- Dragone, C. 1982, *IEEE Trans. Antennas Propag.*, 30, 331–339
- Dragone, C. 1983, *IEEE Trans. Antennas Propag.*, 31, 764–775
- Fowler, J. W., et al. 2007, *Appl. Opt.*, 46, 3444–3454
- Gawronski, W. 2005, in *American Control Conference*. IEEE, FrA11.2
- Gershenson, E., Gol'tsman, G., Gogidze, I. G., Gusev, Y. P., Elant'ev, A. I., Karasik, B. S., & Semenov, A. 1990, Millimeter and submillimeter range mixer based on electronic heating of superconducting films in the resistive state. *Sov. Phys. Supercond.*, 3, 1582
- Goldsmith, P. F. 1998, *Quasioptical Systems* (Piscataway: IEEE). **Chap. 5**
- Greve, A., & Bremer, M. 2010, *Thermal Design and Thermal Behaviour of Radio Telescopes and their Enclosures* (Berlin: Springer). Chap. 9
- Griffin, M. W., Bock, J. J., & Gear, W. K. 2002, *Appl. Opt.*, 41, 4666–4670
- Guilloteau, S., et al. 1992, *A&A*, 262, 624–633
- Gusten, R., et al. 2006, *A&A*, 454, L13–L16
- Hanany, S., & Marrone, D. P. 2002, *Appl. Opt.*, 41, 4666–4670
- Hincks, A. D., et al. 2008, *Proc. SPIE*, 7020, 70201P
- Jaffe, D. T., Harris, A. I., Silber, M., Genzel, R., & Betz, A. L. 1985, *ApJ*, 290, L59
- Jenness, T., Lightfoot, J. F., & Holland, W. S. 1998, *Proc. SPIE*, 3357, 548–558
- Keating, B. G., et al. 2003, *Proc. SPIE*, 4843, 284–295
- Keene, J., Blake, G. A., & Phillips, T. G. 1983, First detection of the ground state $J_K = 1_0 \rightarrow 0_0$ submillimeter transition of interstellar ammonia. *ApJ*, 271, L27
- Kooi, J. W., Chan, M., Phillips, T. G., Bumble, B., & LeDuc, H. G. 1992, *IEEE Trans. Microw. Theory Technol.*, 40, 812
- Korsch, D. 1991, *Reflective Optics* (San Diego: Academic Press)
- Kramer, C., et al. 1998, *Proc. SPIE*, 3357, 711–720
- Lamb, J. W. 1996, *Int. J. Infrared Millim. Waves*, 17, 1997–2034
- Lamb, J. W., & Olver, A. D. 1986, *Proc. IEE-H*, 133, 43–49
- Lawrence, C. R., Herbig, T., & Readhead, A. C. S. 1994, *Proc. IEEE*, 82, 763–767
- Leighton, R. B. 1978, A 10 meter telescope for millimeter and submillimeter astronomy. Final Technical Report for NSF Grant 73-04908
- Leong, M., et al. 2006, *Proc. SPIE*, 6275, 62750P
- Low, F. J. 1961, Low-temperature germanium bolometer. *JOSA*, 51(11), 1300–1304
- Malacara, D. 1992, *Optical Shop Testing* (2nd ed.; New York: Wiley). Chap. 3
- Mangum, J. G., et al. 2006, *PASP*, 118, 1257–1301
- McGrath, W. R. et al. 1997, Superconductive hot electron mixers with ultra-wide RF bandwidth for heterodyne receiver applications up to 3 THz, in *Proceedings of the ESA Symposium 'The Far Infrared and Submillimetre Universe'*, Grenoble, France, ESA SP-401
- Menzies, J., et al. 2010, *Proc. SPIE*, 7739, 77390X
- Moreira, F. J. S., Prata, A., Jr., & Thorburn, M. A. 1996, *IEEE Trans. Antennas Propag.*, 44, 492–499
- Morris, D., Davis, J. H., & Mayer, C. E. 1991, *Proc. IEE-H*, 138, 243–247

- Morris, D., et al. 2009, *IET Microw. Antennas Propag.* 3, 99–108
- Nelson, J. E., Mast, T. S., & Faber, S. M. 1985, *Keck Obs. Rep.* 90, *The Design of the Keck Observatory and Telescope* (Berkeley: W. M. Keck Observatory, Kamuela HI)
- Neufeld, D. A., et al. 2010, Strong absorption by interstellar hydrogen fluoride: Herschel/HIFI observations of the sight-line to G10.6–0.4 (W31C). *A&A*, 518, L108
- Nikolic, B., Hills, R. E., & Richer, J. S. 2007a, *A&A*, 465, 679–683
- Nikolic, B., et al. 2007b, *A&A*, 465, 685–693
- Olberg, E., et al. 1992, *Machinery's Handbook* (24th ed.; New York: Industrial Press), 226
- Padin, S. et al. 2008a, *Appl. Opt.*, 47, 4418–4428
- Padin, S., et al. 2008b, *Electron. Lett.*, 44, 950–952
- Page, L., et al. 2003, *ApJ*, 585, 566–586
- Pearson, J. C., Guesten, R., Klein, & T., Whyborn, N. D. 2000, The local oscillator system for the heterodyne instrument for FIRST (HIFI), in *Proceedings of the SPIE 4013, UV, Optical, and IR Space Telescopes and Instruments*, ed. J. B. Breckinridge, & P. Jacobsen, Munich, Germany (Bellingham: SPIE), 264
- Peterson, J. B., et al. 2000, *ApJ*, 532, L83–L86
- Phillips, T. G. 1988, *Techniques of submillimeter astronomy*, in *Millimetre and Submillimetre Astronomy*, ed. R. D. Wolstencroft, & W. B. Burton (Dordrecht/Boston: Kluwer), 1–25.
- Phillips, T. G., & Huggins, P. J. 1981, Abundance of atomic carbon (C I) in dense interstellar clouds. *ApJ*, 251, 533–540
- Phillips, T. G., & Jefferts, K. B. 1973, A cryogenic bolometer heterodyne receiver for millimeter wave astronomy. *RSci*, 44, 1009
- Phillips, T. G., & Keene, J. 1992, *Submillimeter astronomy*. *IEEE Proc.*, 80, 1662
- Phillips, T. G., & Woody, D. P. 1982, *Millimeter- and submillimeter-wave receivers*. *ARA&A*, 20, 285
- Phillips, T. G., Neugebauer, G., Werner, M. W., & Huggins, P. J. 1977, Detection of submillimeter (870-micron) CO emission from the Orion molecular cloud. *ApJ*, 217, L161
- Phillips, T. G., Kwan, J. Y., & Huggins, P. J. 1980a, Detection of submillimeter lines of CO (0.65 mm) and H₂O (0.79 mm), in *IAU Symp.* 87, *Interstellar Molecules* (Dordrecht: Reidel), 21
- Phillips, T. G., Huggins, P. J., Kuiper, T. B. H., & Miller, R. E. 1980b, Detection of the 610 μ m (492 GHz) line of interstellar atomic carbon. *ApJ*, 238, L103
- Pilbratt, G. L., et al. 2010, *A&A*, 518, L1
- Prober, D. I. 1993, Superconducting terahertz mixer using a transition-edge microbolometer. *Appl. Phys. Lett.*, 62, 2119
- Radford, S., et al. 2008, *Proc. SPIE*, 7012, 70121Z
- Richards, P. L., Shen, T. M., Harris, R. E., & Lloyd, F. L. 1979, A quasiparticle heterodyne mixing in SIS tunnel junctions. *Appl. Phys. Lett.*, 34, 345
- Rowan-Robinson, M., Broadhurst, T., Lawrence, A., McMahon, R. G., Lonsdale, C. J., Oliver, S. J., Taylor, A. N., Hacking, P., Conrow, T., Saunders, W. S., Ellis, R. S., Efstathiou, G. P., & Condon, J. J. 1991, A high-redshift IRAS galaxy with huge luminosity – hidden quasar or protogalaxy? *Nature*, 351, 719
- Rusch, W. V. T. et al. 1990, *IEEE Trans. Antennas Propag.*, 38, 1141–1149
- Russell, R. W., Melnick, G., Gull, G. E., & Harwit, M. 1980, Detection of the 157 micron (1910 GHz) [C II] emission line from the interstellar gas complexes NGC 2024 and M42. *ApJ*, 240, L99
- Ruze, J. 1966, *Proc. IEEE*, 54, 633–640
- Saito, M. 2011, in *Proceedings of the General Assembly and Scientific Symposium 2011 XXXth URSI, Istanbul*, J10.6
- Savini, G., & Hargrave, P. C. 2010, *Proceedings of the 35th International Conference on Infrared, Millimeter and Terahertz Waves* (Piscataway: IEEE), 1–2
- Sayers, J., et al. 2010, *ApJ*, 708, 1674–1691
- Schroeder, D. R. 2000, *Astronomical Optics* (2nd ed.; San Diego: Academic). Chap. 6
- Scott, P. F., & Ryle, M. 1977, *Mon. Not. R. Astron. Soc.* 178, 539–545
- Serabyn, E. 1995, *Wide-field imaging optics for submm arrays*, *ASP Conference Series* 75, 74–81, *Astronomical Society of the Pacific*, Orem UT
- Serabyn, E. 1997, *Int. J. Infrared Millim. Waves*, 18, 273–284
- Serabyn, E. 2006, *Proc. SPIE*, 6275, 62750Z
- Serabyn, E., & Wallace, J. K. 2010, *Proc. SPIE*, 7741, 77410U
- Serabyn, E., Phillips, T. G., & Masson, C. R. 1991, *Appl. Opt.*, 30, 1227–1241
- Stacey, G. J., Lugten, J. B., & Genzel, R. 1987, Detection of interstellar CH in the far-infrared. *ApJ*, 313, 859
- Stark, A. A., et al. 2001, *PASP*, 113, 567–585
- Storey, J., Watson, D., & Townes, C. 1981, Detection of interstellar OH in the far-infrared. *ApJ*, 244, L27
- Swetz, D. S., et al. 2011, *ApJ Suppl.*, 194, 41–
- Tauber, J. A., et al. 2010, *A&A*, 520, A2
- Timoshenko, S., & Woinowsky-Krieger, S. 1959, *Theory of Plates and Shells* (2nd ed.; New York: McGraw-Hill), 57
- Tran, H., et al. 2008, *Appl. Opt.*, 47, 103–109
- Tucker, J. R. 1979, Quantum limited detection in tunnel junction mixers. *IEEE J. Quantum Electron.*, 15, 1234

- von Hoerner, S. 1967, *AJ*, 72, 35–47
- Wengler, M. J., & Woody, D. P. 1987, Quantum noise in heterodyne detection. *IEEE J. Quantum Electron.*, 23, 613
- Wilson, R. N. 1996, *Reflecting Telescope Optics I* (Berlin: Springer)
- Wilson, R. N. 1999, *Reflecting Telescope Optics II* (Berlin: Springer)
- Woody, D. P. 2009, *Submillimeter Astrophysics and Technology: A Symposium Honoring Thomas G. Phillips*, ASP Conference Series, 417, 3
- Woody, D. P. 2011, in *Proceedings of the General Assembly and Scientific Symposium 2011 XXXth URSI, Istanbul*, J10.7
- Woody, D., Serabyn, E., & Shinckel, A. 1998, *Proc. SPIE*, 3357, 474–485
- Zobrist, T. L., et al. 2009, *Proc. SPIE*, 7426, 742613

